PAPER • OPEN ACCESS

Modeling and validation of nonlinear voltage-current characteristics of ITER PF joint sample tested in the SULTAN facility

To cite this article: J Huang *et al* 2022 *Supercond. Sci. Technol.* **35** 025014

View the article online for updates and enhancements.

Modeling and validation of nonlinear voltage-current characteristics of ITER PF joint sample tested in the SULTAN facility

J Huang[1,*] ⓘ, T Bagni[1,2] ⓘ, Y Ilyin[3,4] and A Nijhuis[1] ⓘ

[1] Faculty of Science & Technology, University of Twente, 7522 NB Enschede, The Netherlands
[2] Department of Quantum Matter Physics, University of Geneva, CH-1211 Genève, Switzerland
[3] ITER Organization, Saint-Paul-lez-Durance, France

E-mail: j.huang-2@utwente.nl

CrossMark

Abstract

The International Thermonuclear Experimental Reactor poloidal field (PF) coils are wound into double pancakes with NbTi cable-in-conduit conductors, which are connected by joints in shaking hands lap-type configuration. The coils are operating in pulsed mode with a maximum operating current of 55 kA and peak magnetic field of 6.4 T, utilizing electromagnetic load on the conductors and joints. A series of PF qualification joint samples modified in praying hands configuration is measured in the SULTAN facility. For some samples, a nonlinear voltage-current (VI) characteristic is observed during the assessment of joint resistance. The growth of joint resistance versus the $B \times I$ product is larger than what is expected from the magneto-resistant copper contribution. Two non-homogeneous contact resistance models are developed and combined to quantitatively evaluate the reason for the nonlinear VI behavior in combination with the relevant power dissipation and current redistribution in the joint. The simulations reveal that, for the particular pre-qualification PFJEU2 sample with resistance variation up to 3.5 nΩ, the most probable reason for the nonlinear VI characteristic is a widely spread defective connection between copper sole and shim. The electromagnetic force involves a separation effect on the mechanically and electrically weakly connected parts, resulting into a varying resistance depending on transport current and background field. The hypothesis and models are validated by an experiment on a similar sample PFJEU3 and a post-mortem examination of the PFJEU2 sample.

Keywords: ITER, Poloidal Field, joint resistance, numerical modeling, nonlinear voltage-current, electromagnetic force

(Some figures may appear in colour only in the online journal)

---

1. Introduction

The International Thermonuclear Experimental Reactor (ITER) magnet system contains six poloidal field (PF) coils. These coils are wound with NbTi cable-in-conductors (CICCs). Firstly a double pancake (DP) is wound with two conductors in a two-in-hand winding scheme, then six to nine DPs are stacked together to form a complete PF coil. The conductors within and between the DPs, as well as the conductor terminals to the feeder system and to the jumper in case of bypassing a faulted DP are connected by twin-box lap-type joints. The PF coils are operating in pulsed mode with a maximum operating current of 55 kA and a peak magnetic field of 6.4 T (48 kA and 6.4 T for PF1/6, 55 kA and 4.8 T for PF2-4, 52 kA and 5.7 T for PF5). The windings are subjected to a radial force inwards and an axial force towards to coil mid-plane as the current increasing. The 100 PF joints in total are located at the outer surface of the coils to minimize the impact of the electromagnetic load and allow convenient assembly and maintenance [1].

A campaign of PF joints qualification measurements was carried out in the SULTAN facility (Swiss Plasma Centre) on six PF joints until August 2017, including DC, AC and stability properties. In terms of joint resistance, a nonlinear voltage-current (*VI*) characteristic is observed during the measurements of PFJEU2, PFJEU3 and PFJEU6 samples. Especially for the sample PFJEU2, which was the first trial sample built by a supplier well before the manufacturing procedure was stabilized, a resistance deviation up to 3.5 nΩ is observed for two different electromagnetic load conditions [2]. Similar behavior was also observed in the measurements of some toroidal field joints. A poor current redistribution in the joint with high strand-bundle to copper sole resistance was adopted as the probable reason [3, 4].

The DC properties including the assessment of the joint resistance are simulated with the numerical model JackPot-ACDC, at the University of Twente. The JackPot code has the ability for quantitative analysis of CICCs at a strand level precision in both stationary and transient regimes [5–10]. A twin-box joint is built in the model as an object with three sub-objects consisting of two cables and a copper sole. The cable is implemented following the trajectories of all the strands by the cabling subroutine, while the copper sole is treated as three-dimensional electrical grid with the PEEC technique [11]. A network comprising all meshed elements of the sub-objects is constructed firstly, and accordingly the currents and voltages of the nodes are calculated in response to the transport current and magnetic fields (self-field and externally applied). This allows us to evaluate the individual contributions of cable, copper sole/shim and cable-sole interface to the evolution of the joint resistance. Except for the uncertainty in the heat transfer coefficients, there are no free parameters in the model so the electrical and thermal behavior are mainly depending on the joint configuration and the input contact resistances, the inter-strand, inter-petal and strand to copper sole resistivity, which are derived from experiments.

2. Joint resistance test and simulation

During the manufacturing of the PF joints, the outer surface of the steel wraps, wound around the petals, are removed to get a better electrical contact between the cable and copper sole. In addition, AgSn solder is applied at the contacting interface to further improve the electrical, mechanical and thermal stabilization [12]. The prepared cable end is pressed into a bimetallic box machined from an explosive bonded stainless steel/copper plate to form a termination. A copper shim is inserted between two of these terminations to compensate for manufacturing and positioning misalignments. PbSn soldering is applied at the interfaces between the copper soles and shim, and then the pieces are hold together by two side plates welded to the joint boxes. A cross section of a PF joint including the solder applied between cable, sole and shim, is shown in figure 1 [13].

In the SULTAN facility, besides a maximum sample current of 100 kA, magnet fields are available from both DC and AC coils, orthogonal oriented to each other, as illustrated in figure 1. The DC high-field zone is ∼450 mm long and the AC field has an effective length of ∼390 mm. The samples are vertically inserted into the magnet bore and the terminals are connected to the current leads of a superconducting transformer [14]. The qualification joint samples are modified from shaking hands type (as on the PF coils) to praying hands type to fit the magnet. The configuration of a PF joint sample is shown in figure 2, and the schematic of the SULTAN magnetic fields applied on the joint sample is illustrated in figure 1. The resistance of the joint is measured at sample current $I = 10, 20, 30,$ 40 and 55 kA in background DC fields of 0, 3 and 5 T. Two sets of voltage taps named 'Bottom' and 'Top' taps,are attached to the conductors at 40 and 490 mm distance away from the end of the jointbox, respectively, the average smoothed voltage signal *V* at the two positions are obtained correspondingly, and then the joint resistance is derived as $R = V/I$. For the PFJEU2 sample, after 1000 bipolar load cycles at 6 T/$\pm$ 27.5 kA, the resistances measured at the 'Bottom' position, versus current and background field are shown in figure 3. The joint exhibits a strong nonlinear *VI* characteristic, the resistance increases by 3.5 nΩ as the $B \times I$ product increases from 10 kA and 0 T, to 55 kA and 5 T. Not only this resistance is too high compared to the design requirement of the PF joint resistance ⩽ 5 nΩ [2], but the variation is also not anticipated.

The tests performed in the SULTAN facility, are reproduced and analyzed with the JackPot model. The schematic of the praying-hands lap type PF joint is shown in figure 4, two cables are ideally circular if compared to the realistic oval shape as shown in figure 1. The copper sole and shim with different resistivities are represented with different colors, but the effect of the solder between them is neglected in the simulations. The geometry and resistivity parameters of the modeled PF joint are summarized in table 1, the mask [15] and patch resistivities are defined and explained in the later chapters. The transport current goes from the terminals of Cable A to Cable B, ramping up at $t = 2$ s, with a rate of 2 kA s^{-1} to a
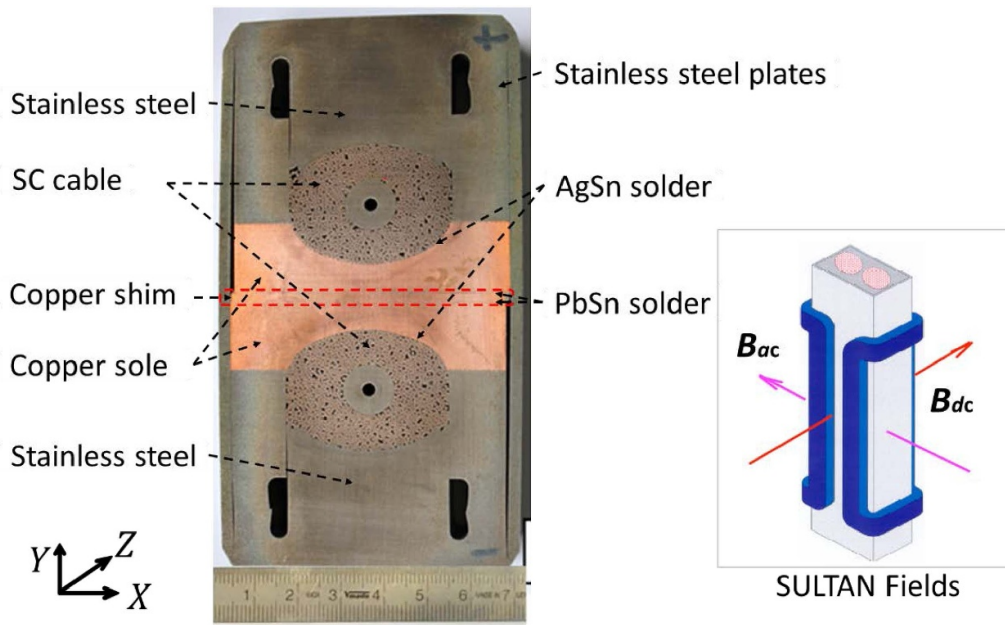
Figure 1. Crosssection of a Poloidal Field joint, including the solder applied between cable, sole and shim, and a schematic of the SULTAN magnetic fields applied to the joint.
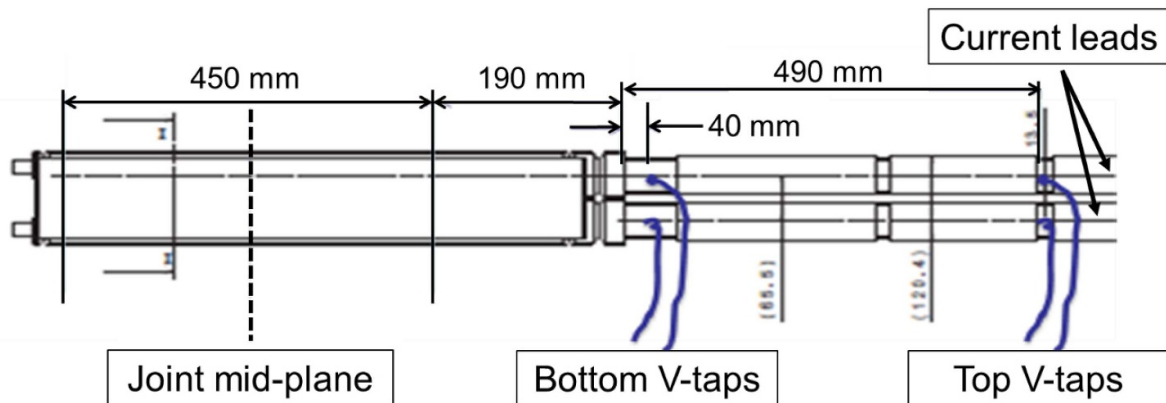

Figure 2. Configuration of the joint sample as tested in the SULTAN facility. The 'Bottom' and 'Top' voltage taps are attached to the conductors at 40 and 490 mm distance away from the right end of joint respectively.

maximum value of 10 kA, then the constant current lasts until $t = 30$ s, as seen in plot (a) of figure 5. The background field is oriented in the X direction. The power dissipation of the whole joint, as well as the three individual components, are calculated with respect to the constant transport current. For example, the power dissipations of joints with different strand to sole resistivities, $\rho_{\mathrm{sj}} = 3 \times 10^{-6}$ and 3×10^{-5} $\mu\Omega\mathrm{m}^2$, are derived and shown in plot (b) and (c) of figure 5. The joint resistance is obtained by dividing the produced power dissipation of the joint by the plateau current squared, $R = P/I^2$. The joint resistances obtained from the simulations for all current-field combinations and the SULTAN measurements are compared in figure 3. It shows that the variation of transport current and magnetic field should have relatively little influence on the joint resistance according to the model results. Even with the incorporated effect of the copper sole and strands' copper magneto-resistance, the computed joint resistance variation is

still far smaller than the maximum 3.5 nΩ obtained from the measurements.

3. Non-homogeneous contact resistance model

According to the characterization and the power distribution as shown in figure 5, the joint resistance derived from the model is dominated by the component of power dissipated in the sole/shim, implying the importance of the resistivity of the copper sole and shim. For the PFJEU2, with a shim layer thickness of 7 mm and low resistivity 0.43 nΩm, the total resistance is reduced by 13%. Another important factor for the power dissipation is the resistivity of the interface between the strands and the copper sole, as demonstrated in figure 5 for two joints with different strands to sole resistivities (ρ_{sj}), 3×10^{-6} and 3×10^{-5} $\mu\Omega\mathrm{m}^2$. Compared to a normal conductor section
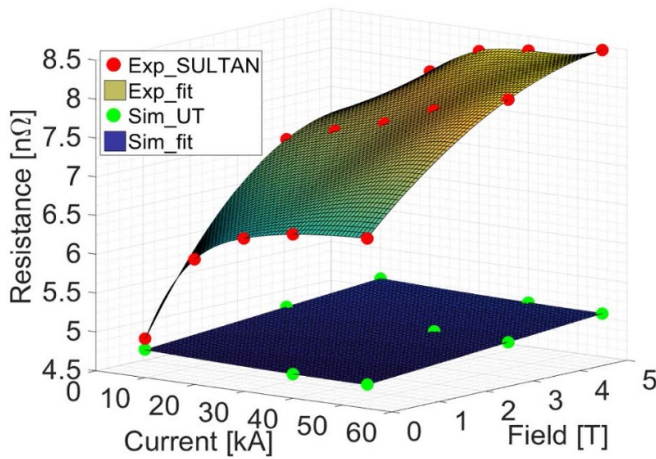
Figure 3. Dependency of the measured joint resistance of PF joint sample PFJEU2 versus the sample current and background field, in comparison with the simulated results in JackPot model.

containing larger voids between strands for helium flow and heat removal, the conductors in the joint section are further compacted and the void fraction is reduced from 34.1 to 24.5% and in addition to the voids occupied by the solder, the actual left void fraction is about $20.0 \pm 0.4\%$ [16]. It is expected that the strands in the cable are tightly compacted, which leads to relatively stable strand to strand resistivity and dissipation in DC conditions. This indicates that the observed nonlinear *VI* characteristic is most likely related to the contact resistivities between the copper sole and shim, or between the copper sole and cable surface, instead of the inter-strand resistances within both cables.

With regard to the two potential causes for the nonlinear *VI* characteristic, two non-homogeneous models are developed to demonstrate the mechanisms behind it. One is the non-homogeneous contact resistance distribution between the sole and shim, focused on two different configurations with integral and discrete shim layers. The corresponding schematics are shown in plot (a) and (b) respectively in figure 6. The other is the non-homogeneous contact resistance distribution between the cable and sole interface, the schematic is shown in plot (c) of figure 6. In the schematics, the non-homogeneous resistance distribution is represented by the discrete sections with different resistivities, the blue color represents the sections with higher resistivity while the white sections are the regions with low resistivity. The non-homogeneity in resistance distribution could also be altered by the dimensions and quantities of the discrete sections.

3.1. Non-homogeneous contact resistance between copper sole and shim

The model concept is based on the assumption that the electrical connection between the copper sole and shim is changed under the influence of the electromagnetic force. For two conductors of the praying-hands type of joint, the transport currents are reversed while the background field direction is the same for both, thus the electromagentic forces

applied on them are in opposite directions, producing a compressing or separating force. In such a case, the resistivity of the discontinuous interface instead of the sole and shim dominate the resistance deviation. In the model, a conservative simplification is made first by treating the separated copper sole and shim as a whole object with an equivalent copper resistivity $\rho_{equ} = 4.0$ nΩm. This resistivity is derived from assuming the same power dissipation as generated in the sole and shim, both having different resistivities.

Based on this joint sole and shim with equivalent resistivity, the non-homogeneous contact resistance model is implemented by adjusting the resistivity and size of the sections with high resistivity, conform the blue regions represented in figure 6. The middle layer with equivalent or high resistivity is still referred to as shim for easy description. Two joint configurations with integral or discretized middle shim layer are considered here, corresponding to figures 6(a) and (b) respectively.

For the shim layer in between both sole parts, the discretization is formed by 11 meshed layers in height (Y) direction, the thickness of one layer is $35/11 = 3.2$ mm. For the integral shim model as shown in figure 6(a), the whole shim layer has homogene high resistivity. For the discrete shim model two discrete configurations, one with seven and one with eleven high resistive sections are considered, the corresponding width is $450/(7 + 6) \approx 35$ mm and $450/(11 + 10) \approx 21$ mm respectively. In total three joint configurations are considered, integral shim, discrete shim with seven and one with eleven high resistive sections are simulated to evaluate the effect of the non-homogeneous sole to shim resistance on the current and power distribution.

Unlike the most probable situation in reality that the contact resistivity and areas of the discontinuous connections change gradually, in the model the resistivity of the individual shim sections is fixed. A factor k_{ρ} is introduced to appoint the resistivity of the shim sections with respect to the normal regions with equivalent resistivity, $\rho_{shim} = k_{\rho} \cdot \rho_{equ}$. For the two cases with integral shim and seven high resistive shim sections, simulatons are performed with 3 T background field and different transport currents, or 40 kA transport current but different background fields. The results are shown in figures 7 and 8 respectively, showing that a nice fit is derived for measured and simulated resistance data by adjusting the shim resistivity by means of the factor k_{ρ}.

In order to catch the increasing tendency of the SULTAN measured data, an increasing k_{ρ} is required for both shim models. As the current increases from 10 to 55 kA at 3 T background field, the k_{ρ} needs to be increased from 25 to 85 for the model with seven discrete shim sections. For the integral shim model the change from 5.4 to 7.0 is relatively small. When the areas of the discrete shim sections are increased, the resistivity is then decreasing and approaching to the shim resistivity of the integral model. A similar tendency is observed as the background field increases from 0 to 5 T and keeps the 40 kA transport current, the k_{ρ} changes from 17 to 85 for the model with seven discrete shim sections, and 4.6–7.3 for the integral shim model.
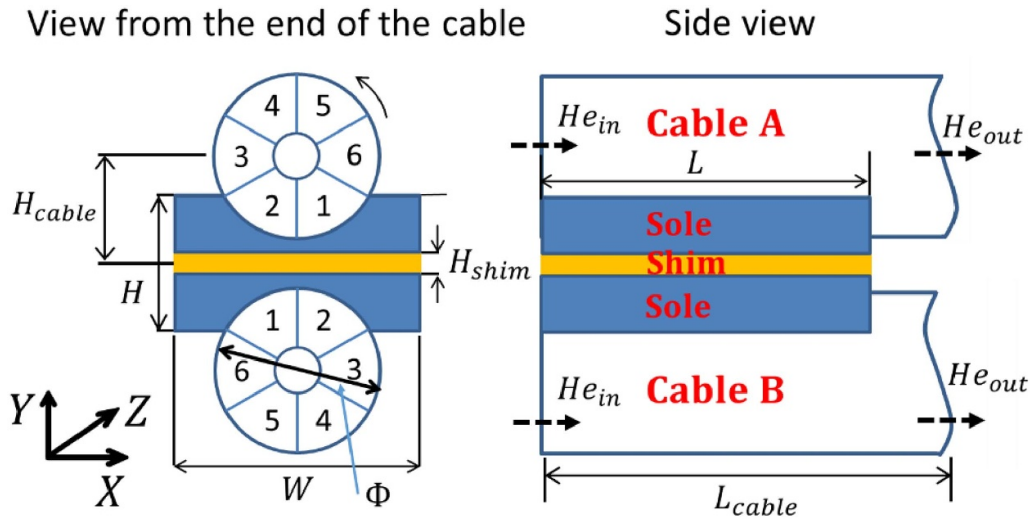
Figure 4. Schematic of the ITER Poloidal Field (PFJEU2) joint in the JackPot model.

Table 1. Geometrical and electrical parameters of ITER Poloidal Field (PFJEU2) joint in model.

Parameter	Value
Sole length L (mm)	450
Sole width W (m)	64
Sole height H (mm)	35
Shim thickness H_{shim} (mm)	7
Cable length L_{cable} (mm)	700
Cable offset to midplane H_{cable} (mm)	26.2
Cable diameter Φ (mm)	35.3
Sole resistivity ρ_{sole} @4.5 K (nΩm)	4.55
Shim resistivity ρ_{shim} @4.5 K (nΩm)	0.43
Equivalent resistivity of joint ρ_{equ} @4.5 K (nΩm)	4.00
Inter-strand resistivity ρ_{ss} ($\mu\Omega$m^2)	1.25×10^{-5}
Inter-petal resistivity ρ_{ip} ($\mu\Omega$m^2)	5.0×10^{-5}
Strand to sole resistivity ρ_{sj} ($\mu\Omega$m^2)	3.0×10^{-6}
Mask resistivity ρ_{mask} ($\mu\Omega$m^2)	50
Patch resistivity ρ_{patch} ($\mu\Omega$m^2)	50

The joint resistance is directly derrived from the power dissipation and thus largely depending on the contribution of the copper sole. For the three defined shim configurations, the integral shim, the discrete shim with seven and eleven high resistive sections, the power distribution across the copper sole length is shown in figure 9 for 40 kA transport current and 3 T background field. A pronounced non-homogeneous distribution is observed for both discrete shim cases and the power is distributed in a few regions along the joint axis. The number of high power regions seems positively correlated but not equal to the quantity of the high resistive shim sections. There are three and five high power regions in the joints with respect to seven and eleven high resistive shim sections.

Considering that the power dissipation is directly related to the current distribution, the current distribution in the sole of the three joint configurations in DC condition, together with the AC condition for comparison, are shown in figure 10. For AC applied field, the joints are subjected to a magnetic field in the Y direction with a ramp rate 1 T s^{-1} for 0.5 s. The present current range is set to ± 1 A to emphasize the distribution itself and ignore the relatively small difference between the magnitudes. The blue color represents the negative current flowing from the far to the near end (figure perspective), the red color represents the opposite current. For DC conditions, the current distribution in the joint is partly affected by the non-homogeneous shim configuration. For AC conditions, the energy distribution in the sole is determined by the resistivity and quantity of the shim sections.

Besides the current distribution, the current density distribution in the copper sole for the three shim configurations are shown in figure 11, when viewed from the position of Cable B. The arrows point in current flowing direction and the color shade represents the density. For Joint 1 with integral shim, the copper resistance and the current are almost uniformly distributed along the joint axis. However, still some local current loops induced at both ends of the sole are observed, due to the masks blocking the electrical connections between the sole and one end of the petals having double contacts with the sole [15, 17]. For Joint 2 and 3, with 11 and seven discrete shim sections respectively, the highest current density flows through a few specific regions, indicated by the dark green color. The current density is not evenly passing all low resistive shim sections, meaning that the current distribution is not only dominated by the resistance distribution in the sole.

This can be explained by the current distribution in the cables. For Joint 3, with seven high resistive shim sections for example, the current density in the sole with respect to the petal current distribution in Cable A, is illustrated in figure 12. In order to emphasize the petal current distribution, two plots viewed from the same angle are compared. The upper plot shows the physical arrangement of the six petals of Cable A, which are labeled from 1 to 6, the lower plot shows the corresponding current distribution. For both plots, the current distributions in the copper sole are identical and the high current
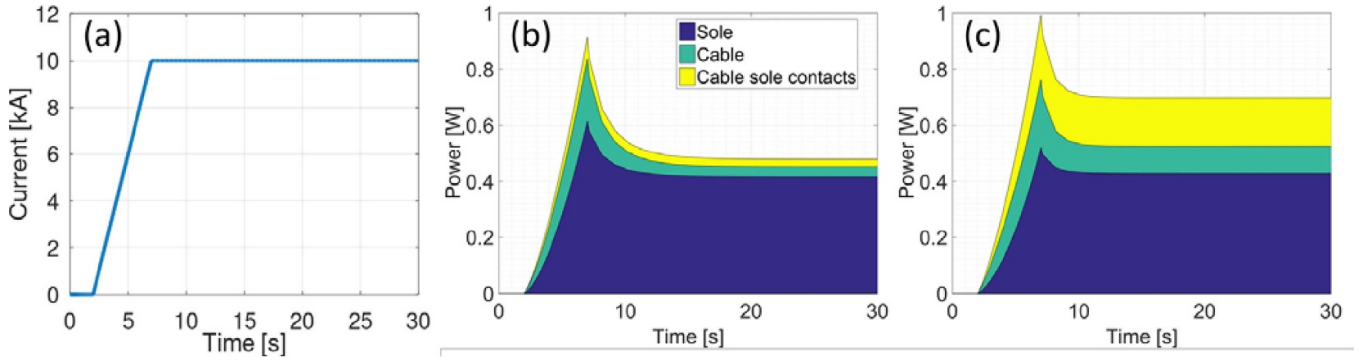
Figure 5. Power dissipation of a PF joint generated during (a) a current ramp to 10 kA constant value. The power distribution is given for the three components, (b) joint with strand to sole resistivity 3×10^{-6} $\mu\Omega\text{m}^2$, (c) joint with strand to sole resistivity 3×10^{-5} $\mu\Omega\text{m}^2$.
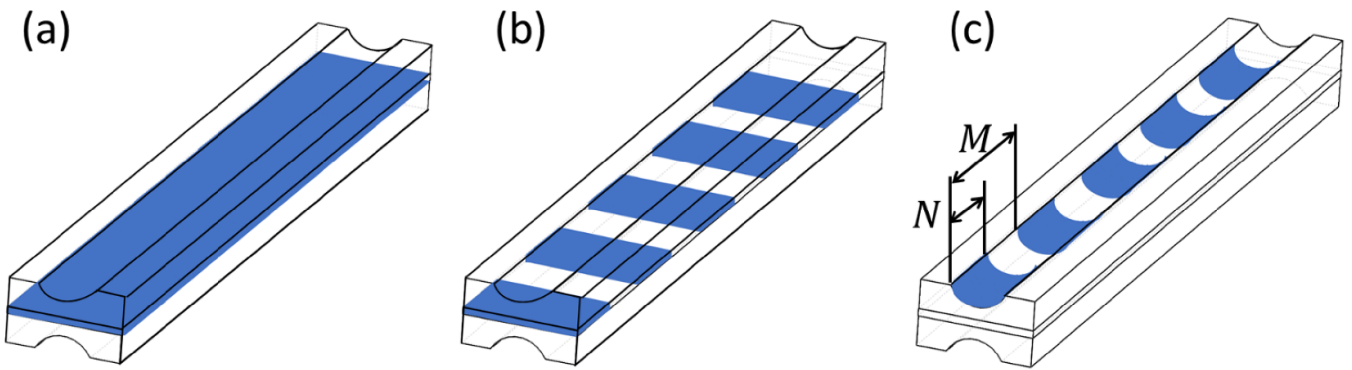

Figure 6. Schematics of the joint models for simulating the non-homogeneous contact resistivities between copper sole and shim, or between strands and copper sole. The blue color represents the high resistive region, (a) integral shim model, (b) discrete shim model, (c) discrete contact resistance between the strands and sole.
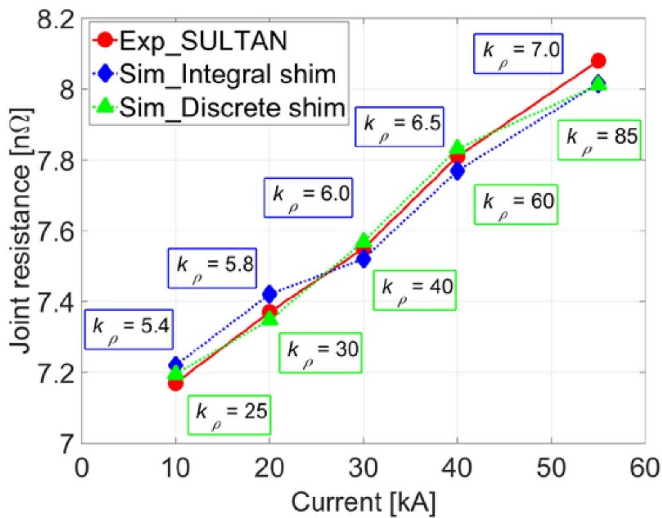

Figure 7. Joint resistances calculated with different shim resistivities in the two non-homogeneous sole to shim resistance models, in comparison with the data measured in SULTAN. The background field is 3 T.
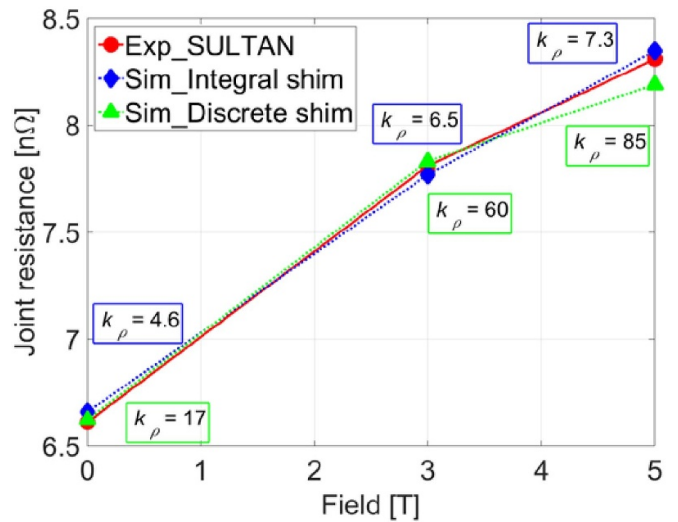
Figure 8. Joint resistances calculated with different shim resistivities in the two non-homogeneous sole to shim resistance models, in comparison with the data measured in SULTAN. The transport current is 40 kA.

regions are named as a, b, c. The magnitude of the strand currents is below 20 A in the jointbox region. For negative transport current from the cable right end, there are positive currents (red color) produced in some strand sections that are in direct contact with the copper sole, especially in the regions with low power dissipation. On first sight it seems there is no resemblance between the shim configuration and the current distribution. The corresponding shim configuration is shown
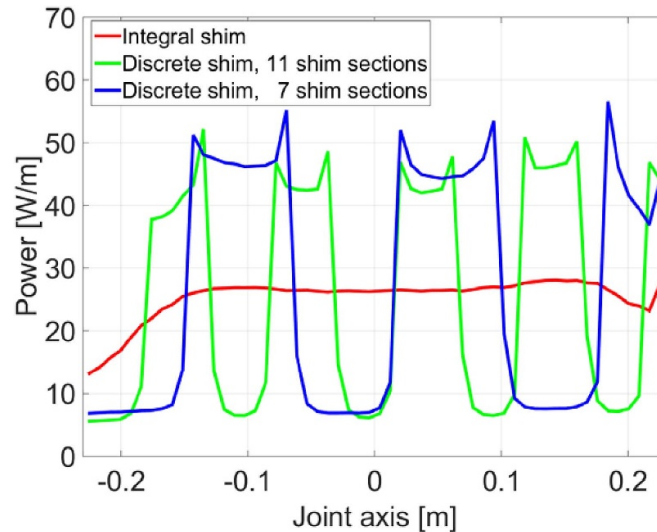
Figure 9. Power dissipation in the copper sole of the joints with different shim configurations, in which the resistance of the joint with integral shim and seven high resistive discrete shim sections are the same.
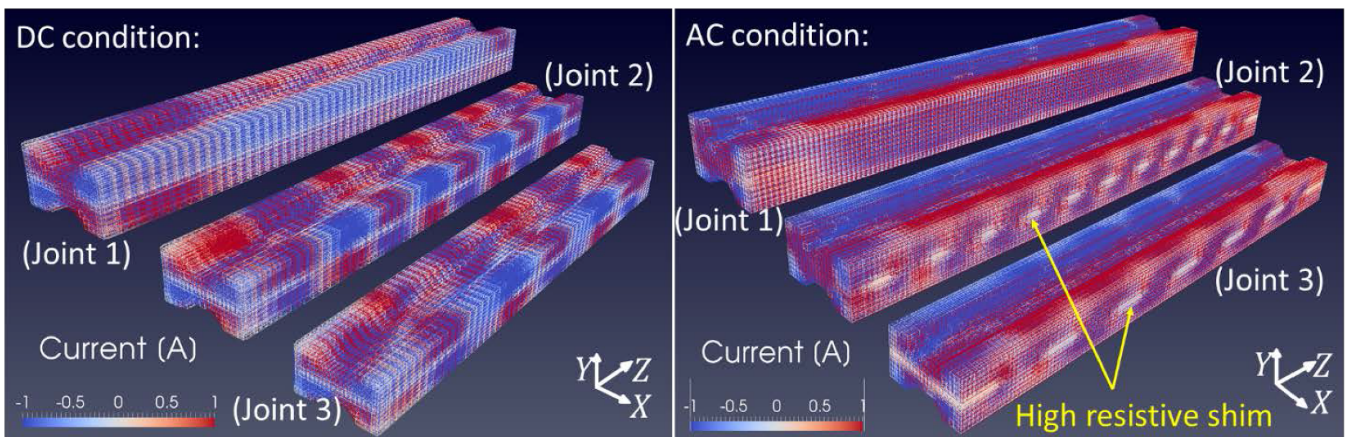

Figure 10. Current distribution in the joints with three shim configurations. With (left) 40 kA transport current and 3 T background field applied in the X direction, in comparison with the AC condition (right) ramp up field applied in the Y direction.

at the bottom of figure 12, using the blue and white color to represent the high and low resistive shim sections respectively. Looking at region a and b for instance, the distributions of the shim sections are actually opposite, while the current densities appear alike.

According to the observation in figure 11, the current transfer mainly occurs in the center of the sole. As a result, the current is mainly carried by one petal, depending on the specific cable rotation with respect to the cable-sole interface. For Joint 3, the currents in petal 1 and 6, petal 2 and 3, and petal 4 and 5 contribute most in regions a, b and c respectively.

3.2. Non-homogeneous contact resistance between strand and copper sole

Another possible reason for the nonlinear *VI* characteristic is a varying contact resistance distribution between strands and copper sole, which is demonstrated with a non-homogeneous contact resistance model. Two levels of contact resistivities

and associated locations, as shown in figure 6(c), are defined as regions (blue color) with higher resistivity, referred to as 'patches'. The size of the patches and the corresponding spatial distribution are determined by two factors M and N, the overall patch ratio is $P_{ratio} = N/M$. Similar to the non-homogeneous sole to shim contact resistance model, only two resistivity levels are considered, the patch resistivity ρ_{patch} which equals to the mask resistivity (ρ_{mask}) [15, 17], and the resistivity of the remaining regions maintaining the strand to sole resistivity (ρ_{sj}). A summary of the resistivity parameters is listed in table 1.

For the case of 3 T background field and transport current increasing from 10 to 55 kA, a comparison between the SULTAN measured joint resistance and the simulated resistance of joints with different patch ratios is shown in figure 13. The patch ratios of 36, 40, 44 and 50% are obtained by setting $N = 4$, $M = 11$, 10, 9 and 8 respectively. The comparison shows that in order to match the increasing tendency of the measured joint resistances, the patch ratio is required to
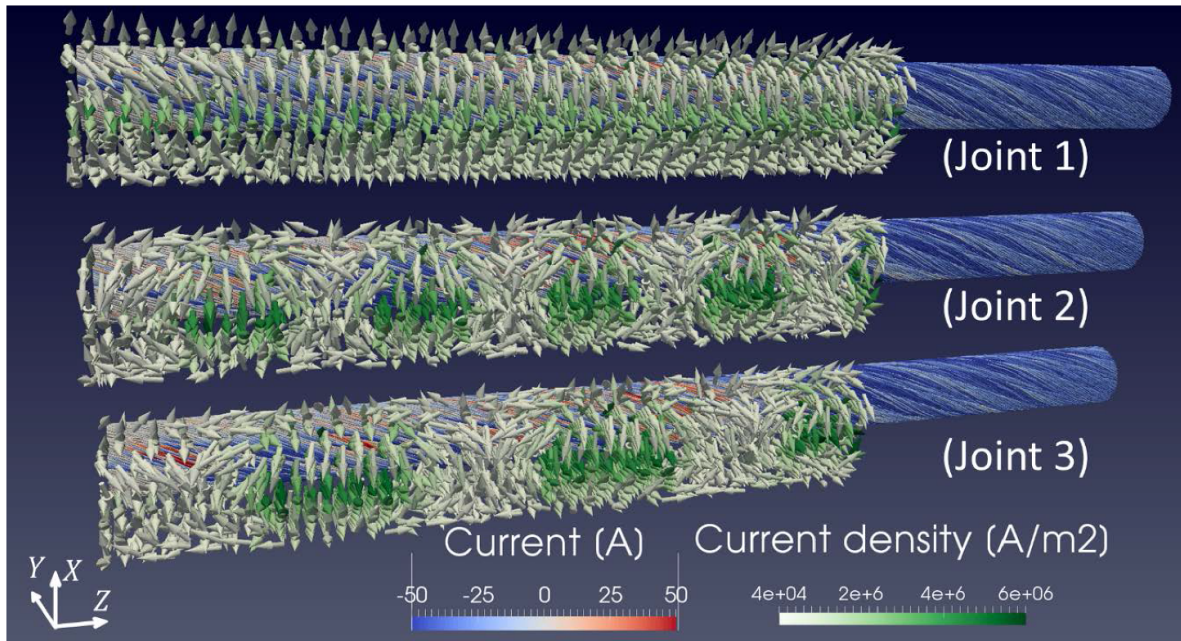
Figure 11. Current density in the copper sole and strand currents in Cable A for joints with three types of shim configurations.
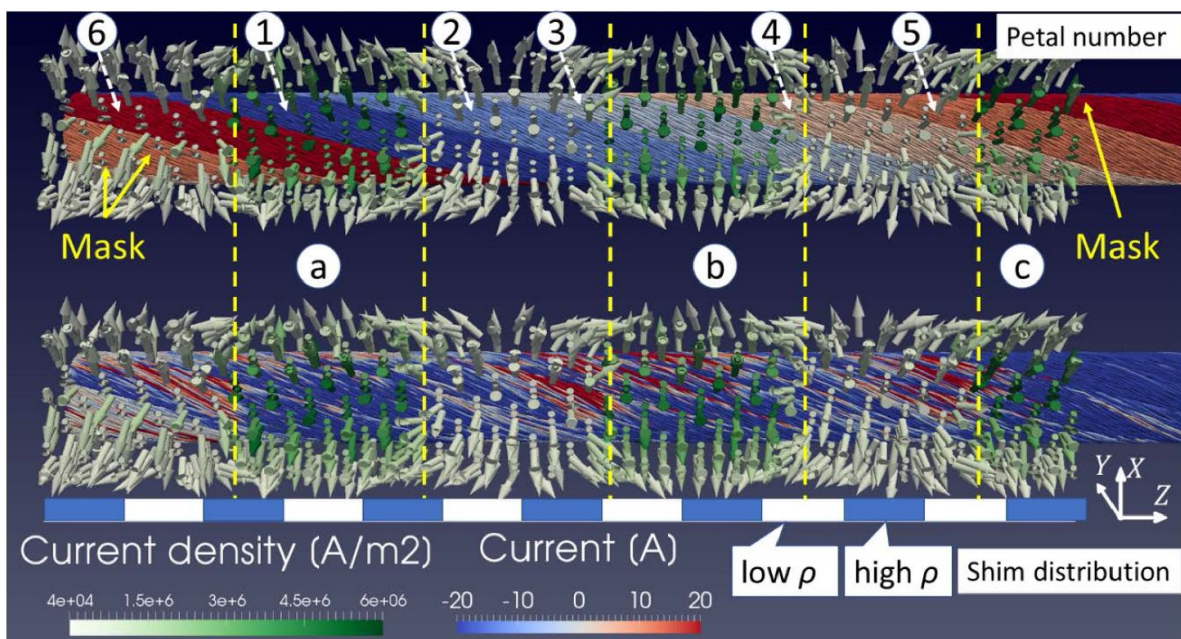

Figure 12. A cross-sectional view from the sole to Cable A of Joint 3, showing the current density in the copper sole with respect to the rotation of the six petals in Cable A (top) and the strand current distribution in Cable A (below). The schematic of the discrete shim configuration is shown at the bottom in blue and white.

increase from 40 to 50%. This means that almost half of the interface between cable and copper sole is in low conductive contact.

Since the calculation of the joint resistance directly depends on the power dissipation, the impact of the patch configuration on the power dissipation is evaluated. Two joints, with and without patches are compared, the patch ratio $P_{\text{ratio}} = 50\%$ ($M = 8$, $N = 4$). The distribution of the power

in the five components, two cables, two cable-sole interfaces and copper sole, is shown in figure 14. Although the non-homogeneous connection is at the interfaces between the cables and sole, the largest effect is still in the copper sole with a non-homogeneous power distribution along the joint axis. The effect is analogous to the periodic distribution of the joint with non-homogeneous sole to shim resistance, as shown in figure 9. In the latter case, the number of power
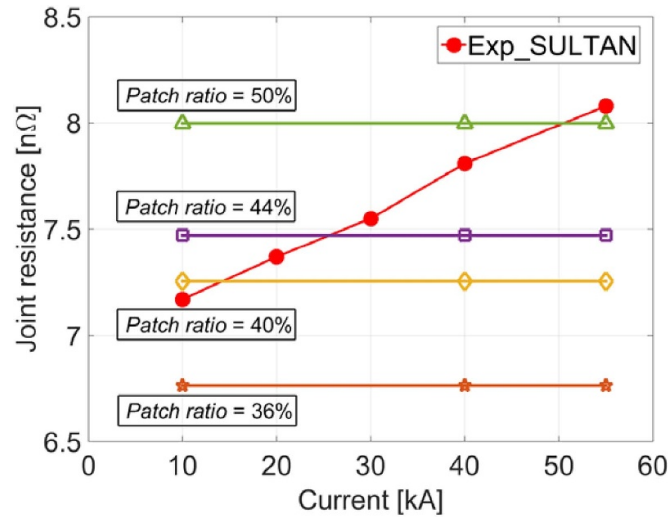
Figure 13. Joint resistances calculated with different patch ratios in the non-homogeneous strand-sole resistance model, in comparison with the data measured in SULTAN. The background field is 3 T.
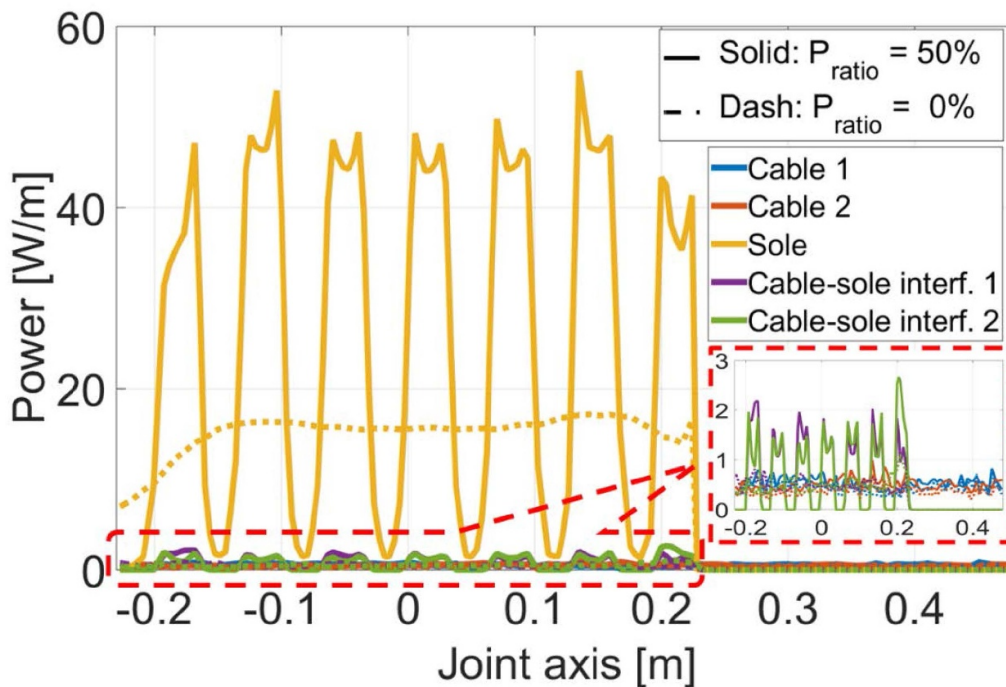

Figure 14. Power dissipation in the five components of joints with patch ratio of zero and 50% respectively, the solid lines represent the joint with 50% patch ratio and the dashed lines represent the joint without patch. At right an enlarged view of the cables and cable-sole interfaces power dissipation.

peaks is determined by the combination of shim configuration and cable rotation together. While in the case of the non-homogeneous strand to sole resistance model, it is solely determined by the patch configuration, with seven power peaks corresponding to the seven patch sections. The power dissipation in the cable-sole interface also interlaces with that in the patch distribution, which is illustrated in the enlarged view in figure 14.

The petal current distribution in Cable A of these two joint cases are compared in figure 15. For the joint without patches, the petal currents transfer into the copper sole smoothly and in a sequence following the petal rotation pattern. While the implementation of the patches prevents such a continuous current distribution, the current plateaus indicate the barrier effect resulting from the patches. However, even though with a patch ratio of 50%, there is still an effective current redistribution in the cable.

A 3D view of the current density distribution of the joint with patches is shown in figure 16, the cable and the copper sole are shown separately to obtain an inside
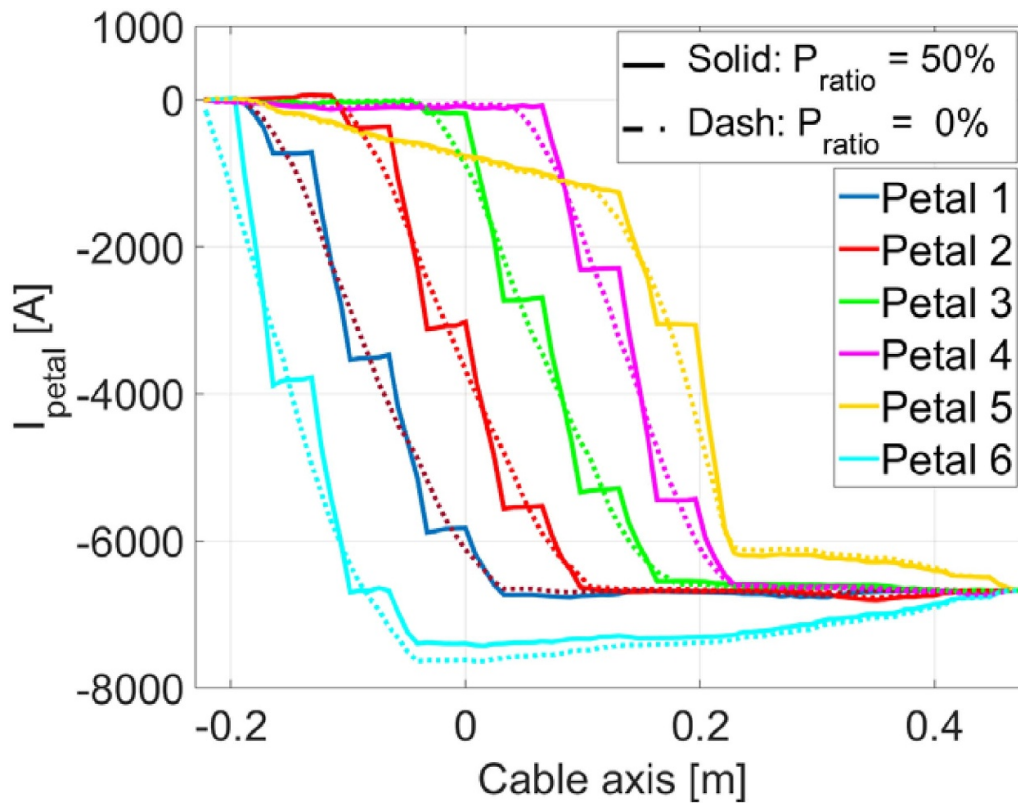
Figure 15. Distribution of the petal currents of the joints with 50% and zero patch ratios.
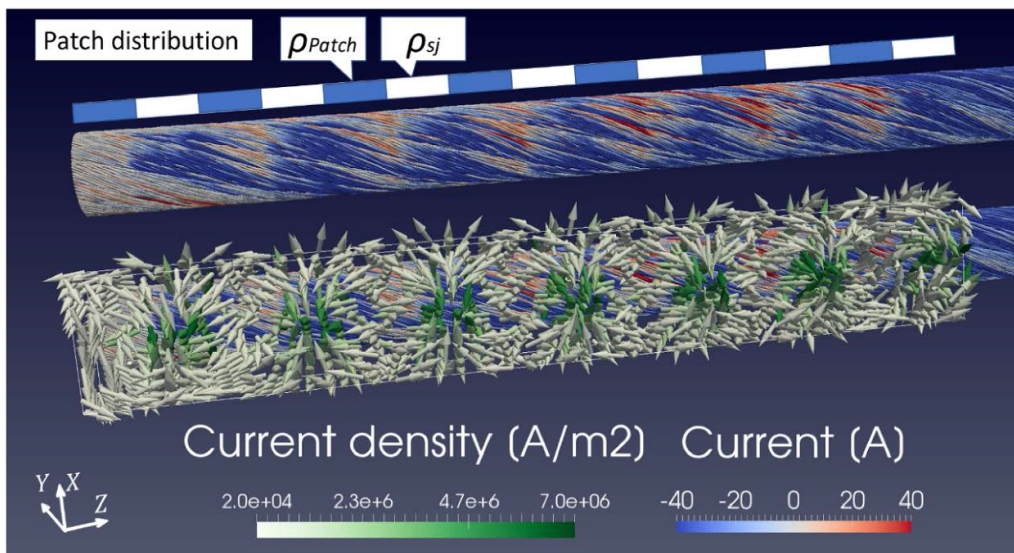

Figure 16. Current density in the copper sole and strand currents in Cable A of the joint with the non-homogeneous strand to sole resistance, the patch ratio is 50% and the patch configuration is shown at the top.

view of the cable to sole interface. The strands in red and blue colors represent the currents flowing in opposite directions indicating that many current loops are induced nearby the patch locations. This is also partly the reason for the periodic current distribution pattern of the cable-sole interfaces observed in figure 14. For the current distribution in the copper sole, the arrows represent the current direction

and the shade of color indicates the density. The majority of transport current is passing through only a few regions, which are directly determined by the patch configurations. In addition, the current is distributed laterally between the mainstream passages, illustrating the phenomenon observed in figure 10 that the positive and negative current occurs alternately.
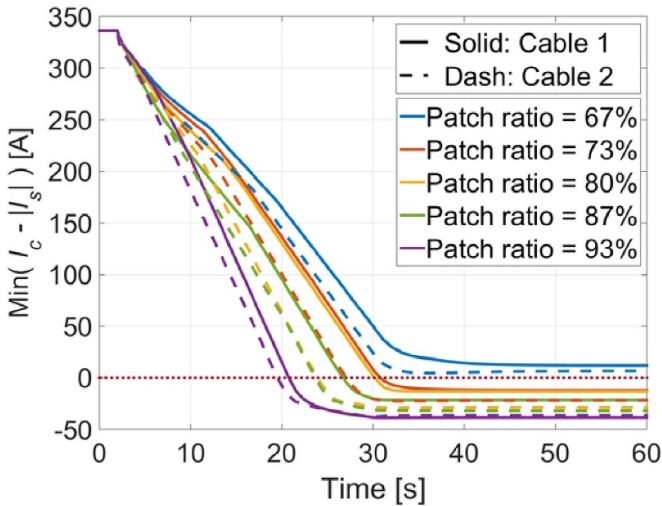
Figure 17. Evolution of the minimum current margin of both cables of the joint for different patch ratios.

Since a quench is not directly detected in the JackPot model, the impact of the patches on the current redistribution and stability is evaluated by means of examining the current margin of the strands. The current margin is defined as $I_{\mathrm{margin}} = \mathrm{Min}(I_c - |I_s|)$ [18], a negative current margin means the strand current exceeds the critical current. In addition, the number of strands with negative current margin is also detected.

In the case of a maximum operating current of 55 kA and 5 T background field, the evolution of the joint resistance and the current redistribution is evaluated by gradually increasing the patch ratio. The patch factor M is set to 15 and as a result there are only three main outlets for the transport current in the cable, the factor $N = 10, 11, 12, 13$ and 14 are corresponding to ratios of 67, 73, 80, 87 and 93% respectively. For the joints with these five patch ratios, the evolution of the current margin in time is shown in figure 17. The time scale here corresponds to the transport current, after a period of 2 s the current increases from zero to 55 kA with a ramp rate of 2 kA s^{-1}, then it remains constant for 30 s. As the patch ratio increases, an earlier current saturation of the strands is observed. For the case of 93% patch ratio, the current saturation occurs at the time instant of about 20 s corresponding to a transport current of 35 kA. Current saturation is observed for all patch ratios except for the smallest patch ratio of 67%. A further examination shows that the number of strands, which get saturated, is 0, 3, 2, 8, and 17 in Cable A and 0, 2, 4, 14 and 19 in Cable B, respectively, for increasing patch ratios. The results reveal that the increasing patch ratios degrade the stability of the joint, a conservative estimation is that a patch ratio up to about 70% may still be tolerated.

4. Analysis and validation

The models reveal that the non-homogeneous contact resistance between either the copper sole and shim, or the strands

and sole, both affect the current redistribution and the power dissipation. However, for any specific configuration, the joint resistance seems independent on the varying input current or background field, if neglecting the effect of the magneto-resistance of the copper sole. Furthermore, the magneto-resistance contribution is much smaller than the resistance variation observed in SULTAN measurements.

Thus, to explain the non-linear *VI* characteristics within the proposed models, one should assume that the non-homogenous contact resistance is a function of the current as can be seen in figures 7, 8 and 13. The most likely explanation is that the electromagnetic force acting on the joint boxes is the cause of the changing contact status. Indeed, the transport current I and background field B as demonstrated in figure 18, result in the electromagnetic force $F = B \times I$ acting on the two cables in opposite direction. The produced separation effect with respect to the joint boxes interface, is positively dependent on the applied B and I, and probably affects the conductive contact between the cable, sole or shim parts.

This hypothesis is confirmed by the effect of the load cycles on the joint. It can be seen from figure 19 that after the 1000 bipolar cycles at 6 T/$\pm$ 27.5 kA, the joint resistance measured at 40 kA is irreversibly increased by 15%–18% at 0 and 5 T, and by 35% at 3 T.

During the measurements of the pre-qualification PFJEU3 joint sample [19] built by another supplier, a similar non-linear *VI* characteristic was observed although the resistance variation is smaller compared to the PFJEU2 sample and the maximum joint resistance remained within the accepted value of 5 nOhm after load cycles. Considering the direction of the electromagnetic force would be changed if changing one direction of the transport current or magnetic field, $-F = - B \times I$, the joint resistances were measured with opposite transport currents so as to obtain opposite electromagnetic force. The results with different transport current and magnetic field combinations are shown in figure 20. An opposite resistance evolution is observed, which corresponds to the separation and compression effect respectively, and validates the effect of the electromagnetic force on the nonlinear *VI* characteristic.

As seen in figure 1, the AgSn solder and PbSn solder are used in the cable-sole and sole-shim interfaces respectively. A post-mortem examination of the sample PFJEU2 was performed at CERN, to check the soldering conditions [13, 20, 21]. The thickness of the AgSn layer is approximately between 200 and 450 μm, obtained from the microscope Scanning Electron Microscope (SEM) images with 60 times original magnification, the solder is in good connecting conditions. While for the PbSn solder, a defective soldering condition is observed with 100 times magnification, and a further energy-dispersive x-ray spectroscopy analysis is performed on the SEM images to detect the probable discontinuity along the interface, a clear gap is observed between the copper shim and PbSn solder, as shown in figure 21. The separation on this unfavorable solder connection under changing electromagnetic force is the most likely reason for the nonlinear *VI* characteristic. This observation is in line with the prediction obtained from the non-homogeneous contact resistance
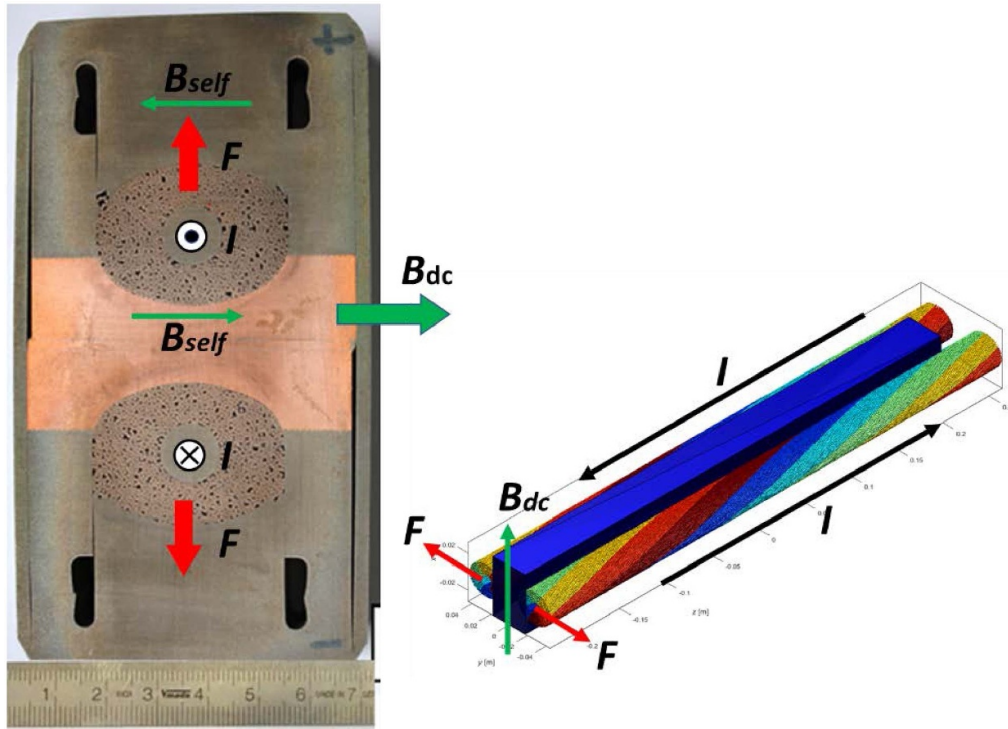
Figure 18. Schematic of electromagnetic force (F) exerted on the SULTAN joint sample, with transport current (I) and background field (B_{dc}).
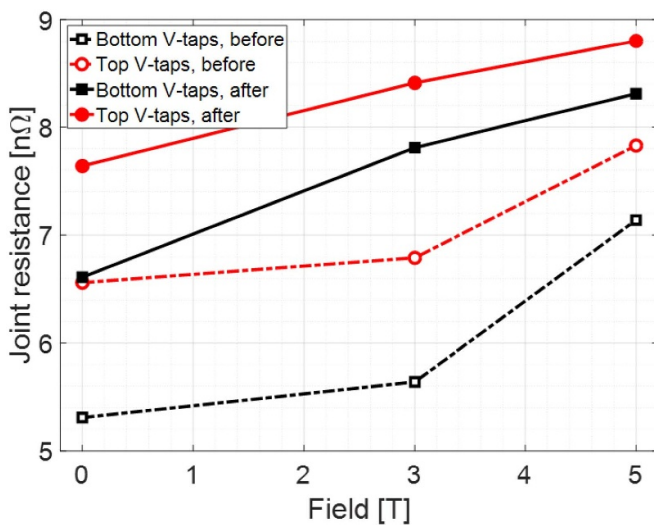

Figure 19. Joint resistance versus different background field at 40 kA transport current, before and after load cycling, for the Top and Bottom voltage taps.
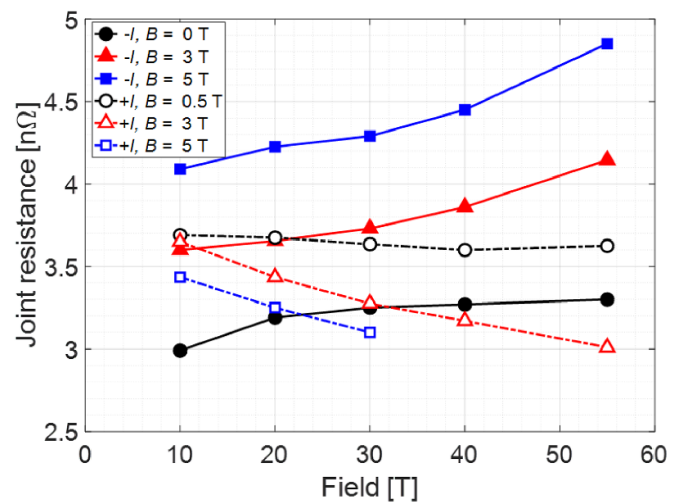

Figure 20. Resistance behavior of PF5 joint sample PFJEU3 measured in SULTAN, for different background fields and positive ($+I$) and negative ($-I$) transport current respectively, with the Bottom voltage taps before loading cycles.

models—a widely spread defective connections between the sole and shim.

The postmortem examination performed on the PFJEU3 sample did not reveal any defects at the soldered interface between the boxes and shim, and the cable void fraction in the middle part of the joint was as low as in the PFJEU2 sample. However, the void fraction appeared to be larger in the portion of the conductors towards the box ends due to larger twist pitch, which could be responsible for the sensitivity of the joint resistance to the EM load. It should be noted, that after the trials with the PFJEU2 and PFJEU3 samples and consequent improvement of the technological process, the next qualification and production samples did not reveal any sensitivity to the EM load [22].
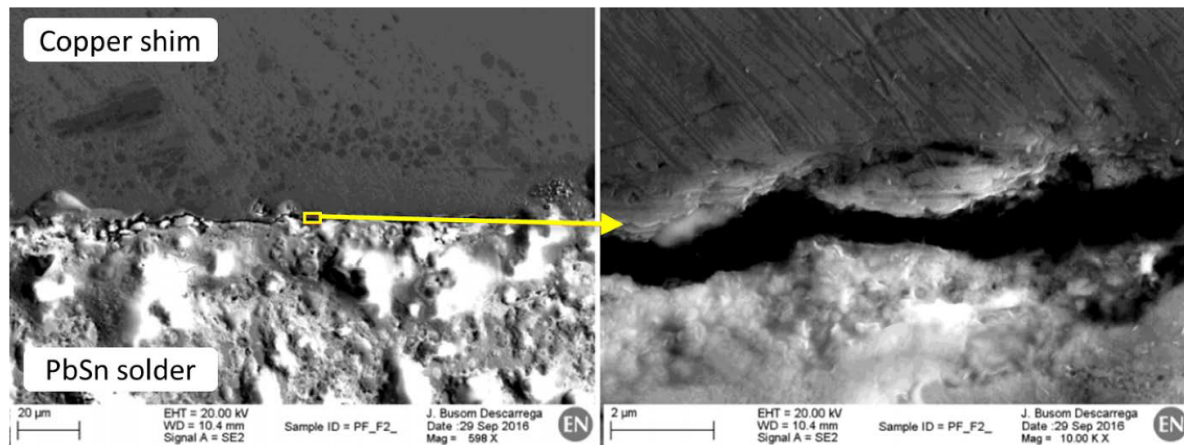
Figure 21. Energy-dispersive x-ray spectroscopy (EDX) analysis performed on the SEM images of the PFJEU2 joint, (left) gap observed at the interface between copper sole and shim, (right) zoom of one specific area.

5. Conclusion

The measurements of the ITER pre-qualification PF joint samples (PFJEU2 and PFJEU3) were performed in the SULTAN facility and unexpected nonlinear voltage-current characteristics were observed during the DC tests. The resistance variation reaches 3.5 nΩ as the transport current and background field increase. The simulations based on the JackPot model show that the joint resistance should be nearly independent from transport current and background field, only a small effect from the magneto-resistance of copper sole and shim is anticipated. The model was updated to emphasize the possible electrical features related to the interfaces between the components of cable, sole and shim. The simulations reveal that the strong nonlinear voltage-current characteristic is most likely a defective connection between copper sole and shim, affected by the electromagnetic force. The weakly connected parts generate a separating or compressing force under a varying electromagnetic force from transport current or background magnetic field, causing a varying resistance correspondingly. Further, on a detailed analysis of the local power dissipation and current distribution in the joint and its strands is presented, allowing a quantitative assessment of the joint stability in AC operating conditions. The model outcome is validated by an experiment on a similar sample PFJEU3 and a post-mortem examination of the PFJEU2 sample.

Data availability statement

The data generated and/or analysed during the current study are not publicly available for legal/ethical reasons but are available from the corresponding author on reasonable request.

Acknowledgments

ORCID iDs

J Huang ⬤ https://orcid.org/0000-0003-1662-4152
T Bagni ⬤ https://orcid.org/0000-0001-8654-783X
A Nijhuis ⬤ https://orcid.org/0000-0002-1600-9451

References

[1] Lim B, Simon F, Ilyin Y, Gung C Y, Smith J, Hsu Y H, Luongo C and Mitchell C J A N 2011 Design of the ITER PF Coils *IEEE Trans. Appl. Supercond.* **21** 1918–21
[2] SWISS PLASMA CENTER 2016 PFJEU2 SULTAN sample, test report
[3] March S, Bruzzone P, Hamada K, Foussat A, Bonito-Oliva A and Cornelis M 2015 Applicability of non-destructive examination to iter TF joints *IEEE Trans. Appl. Supercond.* **25** 4200505
[4] Stepanov B, Bruzzone P, March S and Sedlak K 2015 Twin-box ITER joints under electromagnetic transient loads *Fusion Eng. Des.* **98–99** 1158–62
[5] Van Lanen E P A and Nijhuis A 2010 JackPot: a novel model to study the influence of current non-uniformity and cabling patterns in cable-in-conduit conductors *Cryogenics* **50** 139–48
[6] Van Lanen E P A, Van Nugteren J and Nijhuis A 2012 Validation of a strand-level CICC-joint coupling loss model *Supercond. Sci. Technol.* **25** 025013
[7] Van Lanen E P A, Van Nugteren J and Nijhuis A 2012 Full-scale calculation of the coupling losses in ITER size cable-in-conduit conductors *Supercond. Sci. Technol.* **25** 025012
[8] Rolando G, Foussat A, Knaster J, Ilin Y and Nijhuis A 2013 Performance assessment and optimization of the ITER toroidal field coil joints *Supercond. Sci. Technol.* **26** 085004
[9] Bagni T, Duchateau J, Devred A and Nijhuis A 2018 Quench energy studies in ITER conductors for different magnetic field perturbations with Jackpot and THEA combined models *Supercond. Sci. Technol.* **9** 095001
[10] Bagni T, Duchateau J L, Breschi M and Njihuis A 2017 Analysis of ITER NbTi and Nb3Sn CICCs experimental minimum quench energy with JackPot, MCM and THEA models *Supercond. Sci. Technol.* **30** 095003
[11] Ruehli A E 1974 Equivalent circuit models for three-dimensional multiconductor systems *IEEE Trans. Microwave Theory Tech.* **3** 216–21

[12] Bagrets N 2014 Low temperature thermal and thermo-mechanical properties of soft solders for superconducting applications *IEEE Trans. Appl. Suppercond.* **24** 7800203

[13] Dimitrijevic A and Ilyin Y 2016 *Additional soldering assessment and estimation of percentage of bonding of the PFJS PF Sultan sample (PFJEU2) produced by ASG* Technical Report EDMS NO. 1702063 CERN

[14] Bruzzone P *et al* 2002 Upgrade of operating range for SULTAN test facility *IEEE Trans. Appl. Supercond.* **12** 520–3

[15] Huang J, Bagni T, Ilyin Y and Nijhuis A Pulsed field stability and AC loss of ITER NbTi PF joints by detailed quantitative modelling

[16] Aviles I and Dimitrijevic A 2015 *Void fraction analysis of a PF Sultan sample produced by ASG* Technical Report EDMS NO. 1702063 CERN

[17] Ilyin Y, Rolando G, Nijhuis A, Simon F, Lim B S, Mitchell N and Turck B 2014 Simulations of Twin-Box joints for ITER PF coils *IEEE Trans. Appl. Supercond.* **24** 9001905

[18] Rolando G, van Lanen E P A, van Nugteren J, Offringa W, ten Kate H H J, Ilyin Y, Lim B, Simon F and Nijhuis A 2013 Analysis of heat load, current margin and current nonuniformity in ITER PF coil joints *IEEE Trans. Appl. Supercond.* **23** 4201405

[19] Breschi M, Ribani P L, Cavallucci L and Lotito D 2019 *Analysis of the electrical resistances, thermal resistances, and AC losses of the ITER PF superconducting joints* ITER Report ITER_D_YTF9YG

[20] Langeslag S A E and Dimitrijevic A 2016 *Weld and soldering assessment of the PFJS PF Sultan sample 1 produced by ASG* Technical Report EDMS NO. 1702063 CERN Weld and soldering assessment of the PFJS PF Sultan sample 1 produced by ASG

[21] Langeslag S A E 2016 *Internal soldering assessment of the PFJS PF Sultan sample (PFJEU2) produced by ASG* Technical Report EDMS NO. 1702063 CERN

[22] Ilyin Y *et al* 2018 Qualification program of lap joints for ITER coils *IEEE Trans. Appl. Supercond.* **28** 4201306